JOURNAL OF THE AMERICAN CHEMICAL SOCIETY

pubs.acs.org/JACS

Article

A High-Purity Ethylene Epoxide Stream Produced Using a Supported Electrocatalyst

Jianan Erick Huang,[⊥] Chengqian Wu,[⊥] Yiqing Chen,[⊥] Jiaqi Yu,[⊥] Yuanjun Chen, Huajie Ze, Jaerim Kim, Jinhong Wu, Yang Bai, Xiangyu Ma, Roham Dorakhan, Bosi Peng, Hongmin An, Rui Kai Miao, Min Liu, Lizhou Fan, Sungjin Park, Ke Xie, David Sinton,* and Edward H. Sargent*

Cite This: *J. Am. Chem. Soc.* 2026, 148, 14779−14789

Read Online

ACCESS | Metrics & More | Article Recommendations | Supporting Information

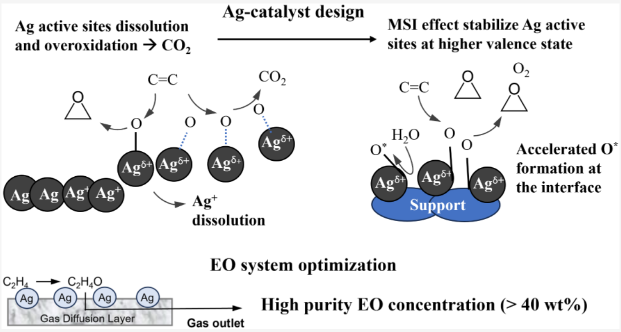

ABSTRACT: Demand for ethylene oxide (EO)—a chemical building block for plastics—exceeds 30 Mt/year. Electrosynthesis of EO from ethylene has, in the highest-activity reports to date, relied on redox-mediated approaches; these lead to chlorinated organic byproducts and high product separation costs due to dilution in solvents as a result of homogeneous electrochemistry. Direct electro-epoxidation is outcompeted by the oxygen evolution reaction (OER) at higher overpotential, causing faradaic efficiencies for EO to drop below 50% above 10 mA/cm^2. We noted that the OER and ethylene oxidation share a common dependency on surface-adsorbed oxygen (M-O*), and that in Pt group metals, the stronger M-O* bonds enhance the kinetics of the OER relative to epoxidation. We therefore considered catalysts, such as Ag, having a less-strongly bound M-O* intermediate. Unfortunately, we found that Ag dissolved easily under anodic bias and that the oxidized Ag surface at a high oxidation state favors the overoxidation to CO_2. We then aimed to leverage metal−support interactions, with our goal being to render the Ag more stable while in its higher oxidation state. An Ag-ZrO_2 catalyst synthesized from a MOF template coupled with the MEA-PTFE system achieves 50% FE for ethylene oxide at 50 mA/cm^2, with a productivity of 460 μmol cm^{-2} h^{-1}. The use of a hydrophilic PTFE separator minimizes system resistance, EO crossover, and hydrolysis, enabling an EO concentration of 48 wt % in the outlet stream at a full cell voltage of 2.1 V in electrolysis paired with HER.

■ INTRODUCTION

The chemical industry contributes 18% of global industrial emissions; half of this is from the production of ammonia and oxygenates, the latter produced via partial oxidation of hydrocarbons through thermal processes at high temperature (>200 °C) and pressure (>10 bar).[1,2] The needed heating and cooling rely today on fossil fuels, and limited selectivity at high temperatures corresponds to undesired overoxidation of the hydrocarbon feedstock. In total, the transformation of ethylene into EO contributes an additional +0.9 to +1.2 tonne CO_2e/ton EO atop the carbon intensity (C.I.) of the ethylene feedstock.

If selective and energy-efficient, electrooxidation could potentially reduce this C.I.[3−5] (Figure 1a and 1b). High overpotential and the low value of oxygen have led to much efforts in the past few years to develop anodic organic oxidation to higher-value products to replace the traditional OER at the anode.[6−9] Such anodic reactions can be paired with valorizing cathodic processes, such as hydrogen evolution, CO_2 reduction, and reductive biomass transformations, such as hydrodeoxygenation.

There has also been much progress in recent years in ethylene electrooxidation, with most reports above 50 mA/cm^2 coming from redox-mediated approaches. Those based on a halide-mediated route lead to chlorinated organics as waste side products and result in high separation costs due to dilute products arising from reliance on homogeneous reactions.[10,11] Direct epoxidation could overcome these separation challenges, but the Faradaic efficiency (FE) higher than 50% for ethylene oxidation in aqueous media has only been reported below 5 mA/cm^2—it becomes dominated by OER at higher current densities.[12] In flow cell configurations, in which gas diffusion electrodes (GDEs) are applied to overcome mass transport issues, the FE has, until now, also diminished to low values at even modest current densities, such as ~2% at 15 mA/cm^2 (Figure S1). Thus, increasing ethylene mass transport

Received: October 10, 2025
Revised: March 17, 2026
Accepted: March 23, 2026
Published: April 1, 2026

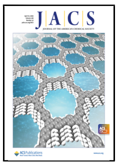

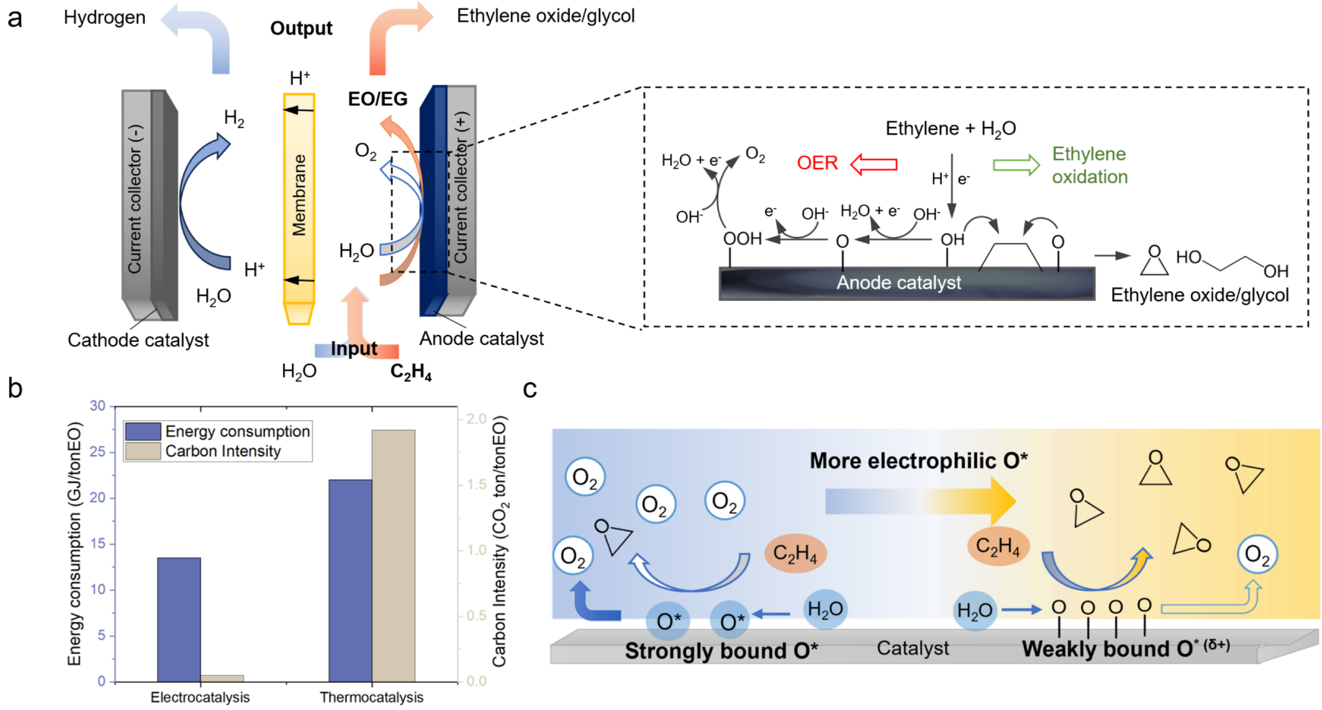

Figure 1. Systems and catalysts for hydrocarbon epoxidation. (a) Ethylene oxidation coupled with hydrogen evolution; the OER competes due to its shared surface intermediates and higher kinetics. (b) Energy consumption and carbon emissions forecast: previously reported thermocatalytic processes (ethylene and oxygen in a thermal reactor) compared with projected electrocatalytic processes once these reach FE > 70%, full cell voltage of 2.1 V, and assuming US grid 2035 electricity is employed. Details in Supplementary note 1. (c) Surface oxygen reaction pathway as a function of adsorption strength.

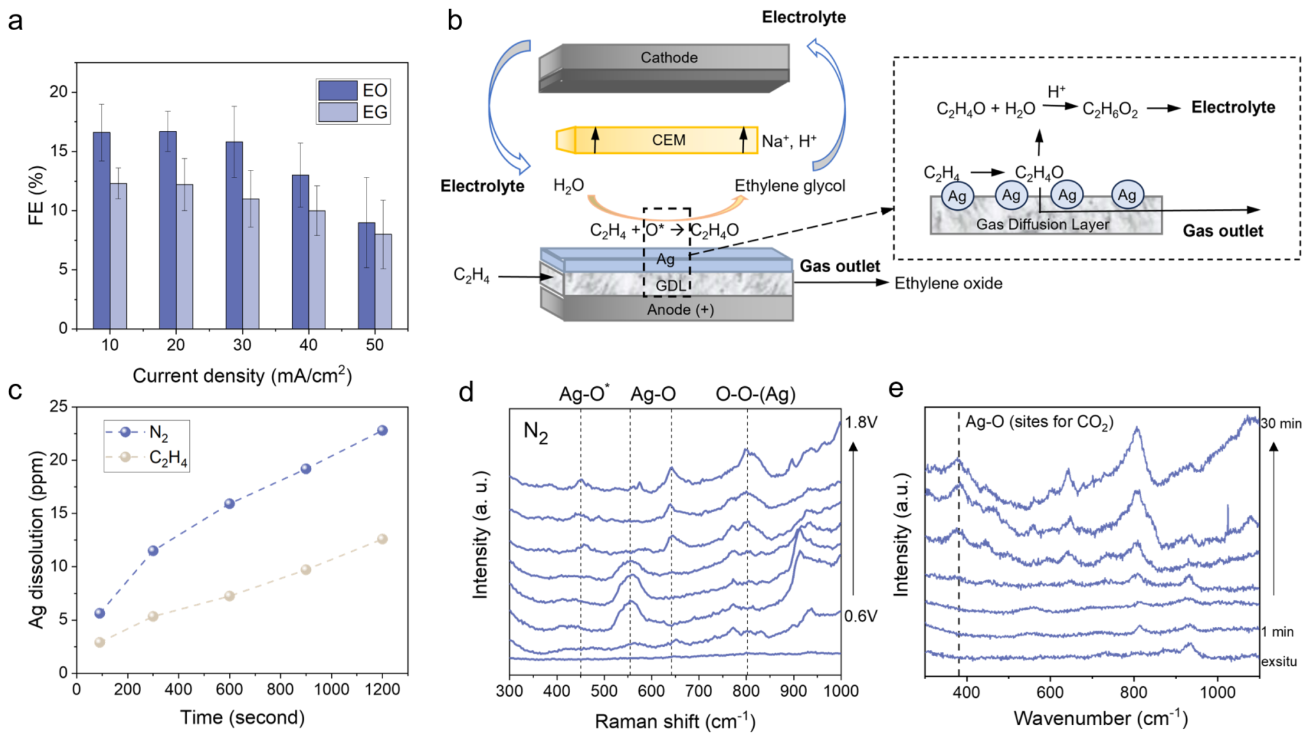

Figure 2. Ag ethylene electrooxidation and operando studies of surface oxygen. (a) FE_{EO} and FE_{EG} on Ag nanoparticles (20 nm) at different current densities. Error bars indicate s.d. (*n* = 3 replicates). (b) Ethylene oxide and glycol branch in the anode chamber: most of the ethylene oxide remaining in the electrolyte is converted to ethylene glycol due to anolyte acidifying. (c) Time profile of Ag dissolution in N_2-saturated electrolyte (pure OER) and C_2H_4-saturated electrolyte (showing ethylene epoxidation with some competing OER). (d) In-situ Raman spectra to investigate the oxygen species evolution on the Ag surface under anodic potentials in N_2- saturated electrolyte. (e) In-situ Raman spectra to investigate the change of the Ag−O feature during extended operation in N_2-saturated electrolyte.

does not, on its own, solve the problem of kinetically favored OER.

It is of interest to look to direct electro-epoxidation of propylene and other olefins that are more nucleophilic than ethylene. Propylene oxidation reports rely on platinum group metal (PGM) catalysts and have mostly operated at modest current densities (<10 mA/cm^2).[13−17] Impressive performance was achieved recently on Pt−Pd alloy catalysts, with high selectivity (∼60% FE) at 50 mA/cm^2 in a water-organic mixture solvent. Unfortunately, the mixed organic-aqueous system led to a high full-cell voltage.[18]

OER and olefin oxidation share a common dependency on surface-adsorbed oxygen, M-O* (Figure 1a). PGM catalysts, such as Pt and Pd, are known to have an optimal binding energy for this M-O* from the point of view of maximizing kinetics in favor of OER. In the case of ethylene, the strong binding of the M-O*, taken together with ethylene's low nucleophilicity, will work against the ethylene oxidation reaction (EOR) outcompeting OER. This prompted us to examine candidate catalysts having less strongly bound M-O* intermediates than those in PGMs (Figure 1c).

■ RESULTS AND DISCUSSION

EOR Performance on Ag Nanoparticles in Flow Cell

We noted that thermocatalysts for EOR are frequently based on Ag, a nonplatinum group metal. Indeed, studies of thermal epoxidation account for good Ag performance by reference to its capacity to stabilize weakly adsorbed electrophilic oxygen required in ethylene oxide formation.[15,19−22] Recently, researchers have reported electrocatalysts using Ag as the active center for both ethylene and propylene electrooxidation to glycol and epoxide, establishing the potential of Ag to become a candidate for the electrooxidation of olefins through alloy and molecular design;[15,23] however, the FE is still not comparable to that of the Pt-group catalyst at high current density.

In cyclic voltammetry (CV) studies (Figure S2), we observed a higher OER onset potential on Ag compared to Pd, consistent with the weak/strong binding affinity trend for oxygen intermediates discussed above. Ag was susceptible to optimization of morphology and electrolyte.[24,25] When we decreased Ag nanoparticle size from 200 to 20 nm and optimized the reaction environment, we detected 17% FE to ethylene oxide and 12% FE to ethylene glycol, taking into account the total amount of each collected from both the gas outlet and the anolyte in unbuffered neutral perchlorate electrolyte (Figure 2a, Figure S3). Even though ethylene glycol was detected as the major product in the anolyte, we discovered through buffered electrolyte tests that ethylene oxide is the first product generated from ethylene electrooxidation (Figures S4 and S5). The anolyte pH keeps decreasing during the electrolysis due to the continuous consumption of OH$^-$ by the anode (Figure S6), which accelerates the hydrolysis of ethylene oxide to ethylene glycol. As a result, a large portion of the ethylene oxide that quickly dissolved in the anolyte was converted to ethylene glycol, while most of the ethylene that exited through the gas channel remained in its original form (Figure 2b, Figure S7).

Unfortunately, we observed that Ag lost EOR performance within 10 min at 30 mA/cm^2 (2.0 V vs SHE), with continuous dissolution observed using Inductively Coupled Plasma (ICP) (Figure 2c). We conducted ethylene oxidation in a post-Ag-dissolution electrolyte, now using carbon paper as the catalyst/electrode, and found negligible FE to ethylene oxide, ruling out the possibility that dissolved Ag$^+$ species played a role in a homogeneous reaction or an electrochemical ethylene oxidation process. Ag-based catalysts have been widely applied in electrochemical reduction reactions and thermal organic oxidation;[26−28] however, the present reaction creates a new challenge for Ag, placing it at high oxidative potential in aqueous media and locally acidic conditions, which encourage its dissolution. We sought to study further how Ag dissolves under epoxidation-relevant electrochemical conditions, hoping to use these insights to delay this process long enough to enable initial (∼1−10 h) studies in membrane electrode assembly (MEA) systems.

Increasing Mechanistic Understanding of Surface Oxygen Reaction Pathways: Studies of Ag Dissolution at High Oxidation States in OER vs EOR

To study the chemical process of Ag dissolution, we conducted CV, X-ray photoelectron spectroscopy (XPS), electrochemical mass spectroscopy (EC-MS), and *operando* Raman spectroscopy. We found via CV that Ag started leaching when it was oxidized from Ag$^+$ to Ag^{2+} at an oxidizing potential higher than 1.1 V vs SHE: the reduction peak of Ag$^+$ to Ag started to diminish (Figures S8 and S9), indicating the loss of Ag$^+$ species after its further oxidation to +2 or higher states. We studied the possibility that a lattice-oxygen-mediated OER process was occurring after Ag^{2+} leaching. The potential (1.6 V vs SHE) for efficient ethylene oxidation above 10 mA/cm^2 (Figure 2a) occurs well above the potential (1.1 V vs SHE) that triggers Ag dissolution.

Upon the introduction of ethylene into the reaction, Ag dissolution is suppressed by a factor of 2 compared to the case of pure OER (i.e., in which no C_2H_4 is in the feed gas) (Figure 2c). We hypothesize that C_2H_4 can scavenge the surface of O*, such that lattice oxygen can no longer proceed. To verify this, we compared CV redox peaks of Ag in N_2- and C_2H_4-saturated electrolytes and found them was unchanged (Figures S8 and S9). This rules out the possibility that C_2H_4 is adsorbing on the metallic or Ag$^+$ sites—a reaction mechanism different from that on Pd, which involves metal−carbon bonding (Figure S10)—and prevents the further promotion to the unstable Ag^{2+} oxidation state. This motivated us to pursue further the hypothesis that C_2H_4 instead consumes the surface-bound O* before it can participate in lattice oxygen evolution, which would accelerate the catalyst dissolution.

To clarify the change of Ag oxidation states, we conducted XPS for Ag, with Ag_2O as a control sample, before and after the reaction. The results show that, once the potential exceeds ∼1.0 V vs RHE, both Ag and Ag_2O evolve toward similar higher-valent Ag$^{\delta+}$ surface states ($\delta > 1$), which are slightly more oxidized than the as-synthesized Ag_2O (Ag$^+$). This indicates that Ag_2O also undergoes surface reconstruction rather than remaining a stable oxide phase (Figure S11). We then conducted ^{18}O isotope-labeling experiments using a $H_2{}^{18}O$ electrolyte coupled with EC-MS to gain further insight into the oxygen pathways during the OER and EOR on Ag. The Ag catalyst is first preoxidized in $H_2{}^{16}O$ to form a fully oxidized surface (Ag$^{\delta+}$) and then tested in $H_2{}^{18}O$ electrolyte. The results reveal that both lattice-oxygen evolution and surface-adsorbed oxygen reactions contribute under anodic conditions on Ag (Figure S12). However, ethylene oxidation incorporates a higher fraction of electrolyte-derived ^{18}O

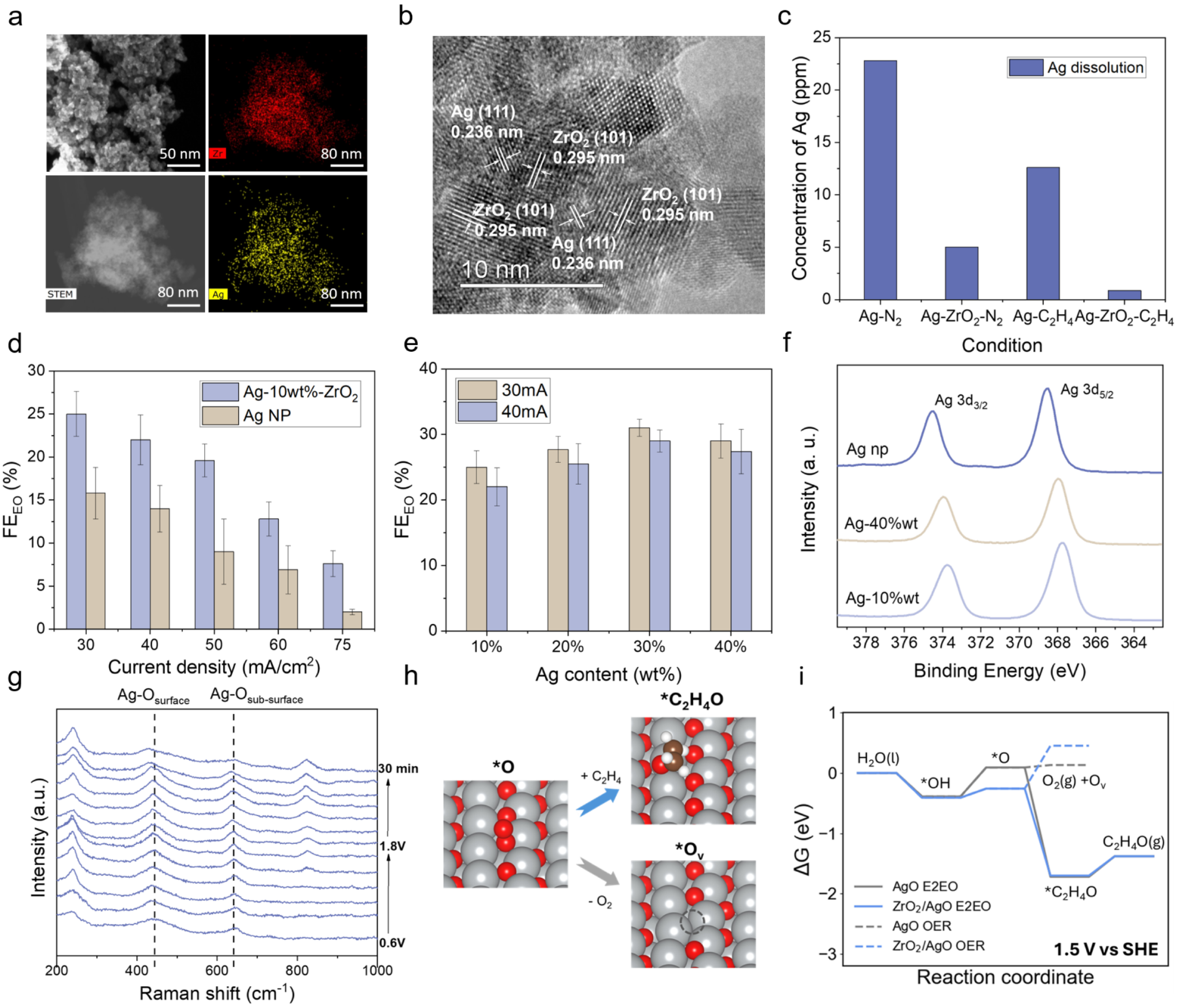

Figure 3. Experimental and DFT studies of Ag-ZrO_2 catalysts. (a) STEM images of Ag-ZrO_2 and EDX demonstrate a uniform distribution of Ag on top of ZrO_2. (b) TEM image of Ag-ZrO_2. (c) Comparison of dissolved Ag for Ag nanoparticles vs Ag-ZrO_2 in N_2- and C_2H_4-saturated electrolyte after operating under 30 mA/cm^2 for 15 min. (d) Comparison of FE_{EO} for Ag 10 wt %-ZrO_2 vs Ag nanoparticles (20 nm) at different current densities. (e) Comparison of FE_{EO} for Ag-ZrO_2 at different Ag loadings. (f) XPS to study the Ag oxidation state in different Ag-based catalysts. (g) In-situ Raman spectra to investigate the oxygen species evolution on the Ag-ZrO_2 surface under anodic potentials in C_2H_4-saturated electrolyte. (h) Bifurcation step for ethylene oxidation and OER. Ag, silver; O, red; C, brown; and H, white. (i) DFT comparison of the OER pathway and epoxidation pathway on Ag and Ag-ZrO_2 surfaces.

compared to OER, suggesting that the dynamically adsorbed oxygen species react more readily with ethylene than with OER. Having established the reaction mechanism, we then examined the origin of catalyst deactivation, which is marked by the sharp increase of complete oxidation toward CO_2 with a concurrent decline of both epoxidation and OER selectivity during extended operation.

To study this catalyst decay mechanism, we turned to investigate the evolution of surface Ag–O features that control the selectivity through *in situ* Raman spectroscopy in N_2- vs C_2H_4-saturated electrolyte with varying potentials and operating time (Figure 2d and 2e, Figure S13). As the potential increases from 0.6 to 1.0 V vs SHE, a broad peak emerges that is centered at 550 cm^{-1}, corresponding to the formation of Ag_2O. This peak begins to diminish and eventually disappears above 1.1 V vs SHE, indicating the loss of these oxide species at high overpotentials as the system transitions into the EOR and OER region. This coincides with two features appearing at 450 cm^{-1} and 650 cm^{-1}. The disappearance of 550 cm^{-1} above ∼1.1 V vs SHE and the concurrent emergence of a ∼650 cm^{-1} band indicate further oxidation of Ag beyond Ag^+, as confirmed by XPS and CV, which showed higher Ag oxidation states accompanied by surface leaching and reconstruction. We therefore assign the higher-frequency feature to a more strongly bound, higher-valent Ag–O species with subsurface or lattice-like character, which is more stable than the dynamically dissolving surface Ag–O species.[29,30] The surface Ag–O signal (450 cm^{-1}) is much less intense, with the ethylene-saturated electrolyte showing even less signal, likely due to the continuous consumption of the surface oxygen species from epoxidation. The peaks centered near 800 cm^{-1} in the pure OER case are assigned to increasing surface O–O species.[30−32] During extended operation, we observed that the surface Ag–O vibration feature at 450 cm^{-1} progressively diminishes and is replaced by a more red-shifted band centered at 380 cm^{-1}. The emergence of this peak coincides with the onset of increased CO_2 formation and loss of both epoxidation and OER activity (Figures S12 and S33), suggesting a surface Ag−O network with weaker bonds and more reactive surface oxygen.

Taking together the evidence from ICP, XPS, CV, and Raman, with and without C_2H_4, we conclude that ethylene epoxidation preferably involves surface-bound O* intermediates. The shift in selectivity toward CO_2 originates from anodic surface dissolution and the reconstruction of Ag into highly reactive, weakly bound Ag−O species, evidenced by the emergence of strongly red-shifted Raman features (~380 cm^{-1}), which promote overoxidation of epoxide intermediates and subsequent C−C bond cleavage, rather than from complete Ag dissolution or simple loss of active surface area.

Under thermocatalytic conditions on metallic Ag, epoxidation is commonly described as proceeding via a metal-stabilized oxametallacycle intermediate involving persistent Ag−C bonding. In contrast, under anodic electrochemical conditions, the Ag surface exists predominantly as oxidized $Ag^{\delta+}$ species with high O* coverage, which reduces π-backdonation to ethylene and disfavors strong Ag−C coordination. Based on the Raman, XPS, CV, and DFT results, we propose an electrochemical epoxidation mechanism that is more likely to proceed via electrophilic attack of surface O* on the C═C bond to form a transient $O{-}C_2H_4$ intermediate, rather than through a stabilized metal-inserted oxametallacycle.

Metal−Support Strategy to Render Ag Stable in High Oxidation States

To improve the selectivity at a higher current density region (~50 mA/cm^2), at which potential the Ag is prone to be oxidized to higher oxidation states. We turned to strategies to stabilize Ag in the higher oxidation state. In the allied fields of both thermo- and electrocatalytic oxidation, including oxidative dehydrogenation, CO oxidation, glycerol oxidation, and OER, support effects have been used to achieve similar ends.[33−36] The metal−support interaction (MSI) stabilizes metal active sites and affects interfacial processes—including charge transfer and intermediate formation—mechanisms that influence the selectivity of reactions.[37,38] We studied both ZrO_2 and CeO_2 as metal oxide supports, as these are known to improve the dispersion of metal sites and enhance catalytic activity and stability in oxidation reactions.[36,39,40] We employed hydrothermal synthesis (Methods) and found, via microscopy, that Ag nanoparticles are impregnated within and near the surface of the metal oxide support (Figure 3a and 3b, Figure S14 and S15).

We first studied, using ICP, the rate of Ag dissolution under the same conditions as those in pure-Ag studies. We found that the rate of Ag dissolution is suppressed by more than 10× during the highest dissolution period (the first 15 min of the reaction) in the case of the ZrO_2 support (Ag 10 wt %) compared to the pure Ag case (Figure 3c).

We then tested each metal oxide support in its pure form and found no measurable activity in ethylene oxidation. When we impregnated Ag at 10 wt %, these catalysts demonstrated superior performance compared to their pure Ag counterparts across the current range of 30−75 mA/cm^2 (Figure 3d). We optimized Ag loading on each support and found the best loading to be 30 wt %, yielding an ethylene oxide FE of 26% at 40 mA/cm^2 on CeO_2-supported Ag; ZrO_2-supported Ag at 30 wt % exhibited a higher ethylene oxide FE over 30% at 40 mA/cm^2 (Figure 3e and Figure S16). From ex situ XPS, we found that the oxidation state of Ag is increased when we embed it in the support, suggesting electron transfer between the Ag and ZrO_2 (Figure 3f). The best performance, achieved near 30 wt %, can be accounted for by the goal of maintaining a balance between a high density of Ag-ZrO_2 interfacial sites—which we posit serve as the selective ethylene oxidation sites—and ensuring sufficient Ag coverage for conductivity, without excessive particle growth that would compromise unduly the desired MSI effects. Compared to CeO_2 support with a fast redox cycle and high O mobility that could trigger oxygen evolution (Figure S16), ZrO_2, a nonredox oxide, electronically stabilizes Ag species at higher oxidation states while suppressing the lattice oxygen evolution pathway.

To study the role of ZrO_2, we used density functional theory (DFT) to consider reaction pathways on Ag vs Ag-ZrO_2. We found that the formation of surface-adsorbed O* is the rate-determining step for both the ethylene oxidation pathway and the OER pathway on Ag. We calculated the reaction energy barriers of the oxygen intermediates at Ag-ZrO_2 interfacial sites. Our focus is on the interfacial chemistry; since the barriers are governed by the local bonding environment, the stacking order does not affect the conclusions. DFT results suggest that the introduction of ZrO_2 near the Ag surface increases the barrier in OER ($O^* \text{ to } O_2(g) + O_v$), corresponding to vacancy formation that leads to lattice oxygen participation[41] (Figure 3h and 3i, Figure S17−19). The support also lowers the energy barrier in the rate-determining step (O* formation) in ethylene oxidation on AgO (111), rendering the $C_2H_4O^*$ formation step more favorable than OER in both lattice oxygen and adsorbed oxygen pathways (Figure S20).

Experimentally, ZrO_2-supported Ag maintains more persistent features at 450 and 650 cm^{-1} over time (Figure S22). The peak centered at 450 cm^{-1} is more pronounced than that on pristine Ag, even at lower potential, indicating the presence of high-valence $Ag^{\delta+}$-O on the surface and a higher oxygen coverage, consistent with the DFT results suggesting a faster surface oxygen formation rate at the Ag-ZrO_2 interface. The intermediate $Ag{-}O_{surface}$ configurations also stabilize over an extended period of operation, and no trace of a red-shift toward 380 cm^{-1} state that leads to performance decay is observed. Through ^{18}O isotope labeling EC-MS, Ag-ZrO_2 exhibits a pronounced suppression of mixed-isotope O_2 signals ($m/z = 34$), demonstrating effective inhibition of lattice-oxygen-mediated OER pathways (Figure S21). This suppression correlates with enhanced catalyst stability and selective ethylene oxidation, consistent with the interfacial stabilization of $Ag^{\delta+}$-O species seen in Raman spectra and predicted by DFT.

Optimization of Ag-ZrO_2 Structure Increases Performance at High Current Densities

The peak FE to ethylene oxide for the Ag-ZrO_2 catalyst reached 31% at 30 mA/cm^2, but thereafter exhibited a decreasing FE in the higher current region. Previous analysis suggests that the interface between Ag and oxide support serves as the active sites that facilitate oxidation on ethylene. We sought to improve the FE at higher current densities by further improving the Ag dispersion on ZrO_2 at the nanoscale and maximizing the metal−support interface.

We employed the Zr-based metal−organic framework UiO-66 as a template for catalyst synthesis, followed by Ag

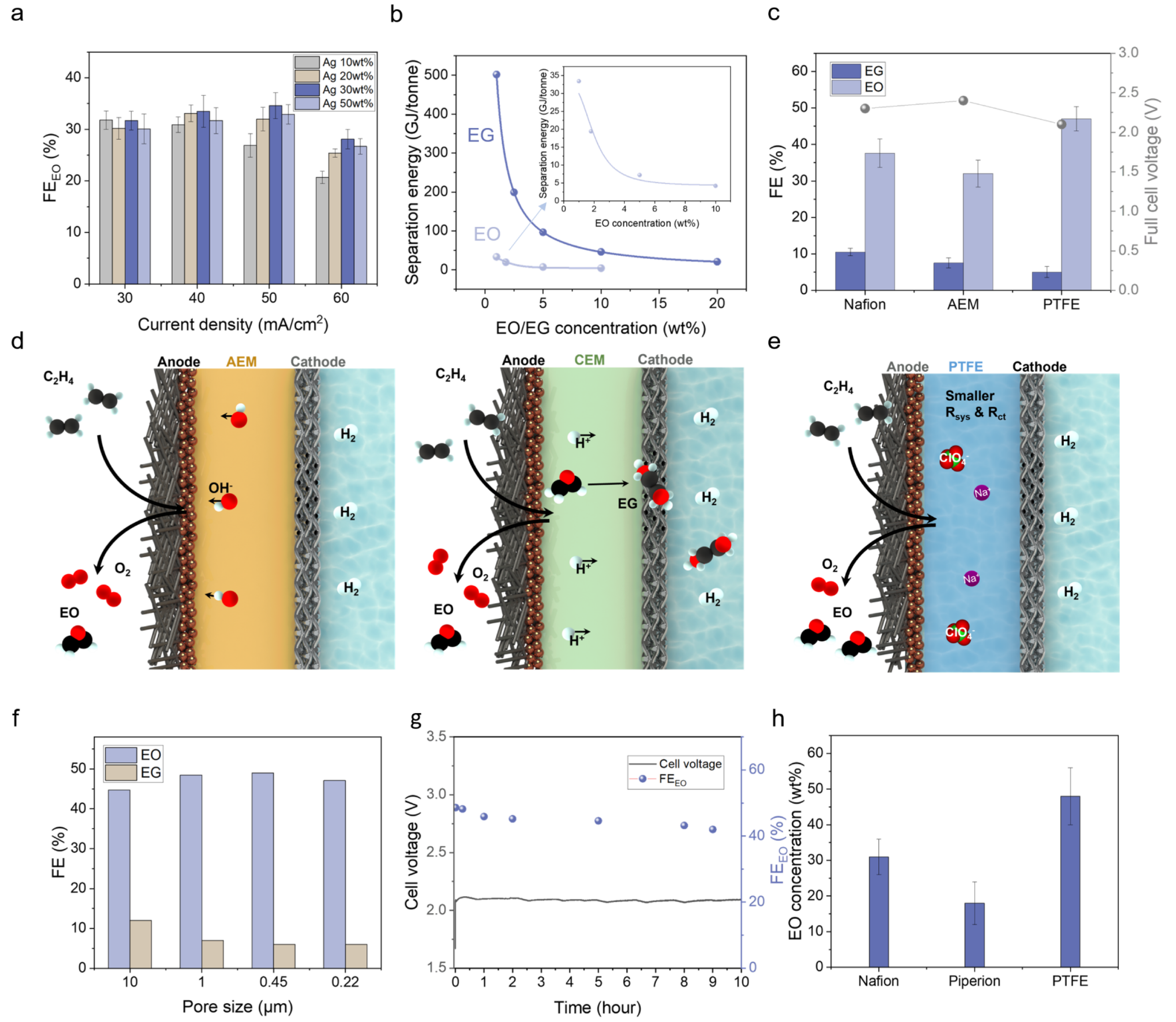

Figure 4. Optimization of MOF-Ag-ZrO$_2$ catalyst, including in an MEA system designed to maximize the output concentration and minimize energy cost. (a) Optimization of loading Ag-ZrO$_2$ catalyst at different current densities. (b) Sensitivity of separation energy of ethylene glycol and ethylene oxide with respect to concentration. (c) Comparison of FE$_{EO}$ and FE$_{EG}$ in MEA with different membranes and crossover of ethylene oxide and glycol to the catholyte when using different membranes. (d) EOR coupled with HER in an anion exchange membrane MEA system and CEM system. (e) Zero-gap MEA system EOR-HER with a hydrophilic PTFE membrane and NaClO$_4$ electrolyte supplied from the cathode side. (f) Optimization of EO/EG ratio using different pore sizes of the hydrophilic PTFE membrane. (g) Extended test of Ag-ZrO$_2$ catalyst in the MEA system. (h) Comparison of ethylene oxide concentration collected at the gas outlet using different membrane systems.

impregnation and thermal annealing (Methods). This strategy was designed to anchor Ag$^+$ ions within the porous Zr-MOF framework prior to oxide formation, thereby ensuring intimate nanoscale contact between Ag and the ZrO$_2$ matrix that forms during pyrolysis. Such confinement enables a high density of Ag-ZrO$_2$ interfacial sites upon framework decomposition. Consistent with this design, we observe a highly uniform distribution of Ag nanoparticles on ZrO$_2$ (Figures S23−S26). X-ray photoelectron spectroscopy further reveals slightly higher Ag oxidation states compared to hydrothermally synthesized Ag-ZrO$_2$ at identical loadings, indicating stronger metal−support interactions in the MOF-derived catalyst (Figure S27). As a result, the optimized MOF-templated Ag-ZrO$_2$ achieves a peak ethylene oxide Faradaic efficiency of 35% at an elevated current density of 50 mA cm^{-2} when Ag loading reaches 40 wt % (Figure 4a, Figure S28).

To disentangle the role of particle size from interfacial effects, we compared the Ag nanoparticle size distributions across all catalysts by TEM (Figure S24). Unsupported Ag consists of particles with an average size of ~20 nm, whereas hydrothermally synthesized Ag-ZrO$_2$ contains larger Ag particles in the 50−100 nm range. In contrast, the MOF-derived Ag-ZrO$_2$ exhibits a more uniform Ag dispersion with particle sizes of ~20−50 nm. Although these larger Ag particles are generally expected to exhibit lower activity in ethylene oxidation due to a reduced surface-to-volume ratio, both hydrothermal and MOF-synthesized Ag-ZrO$_2$ nevertheless show markedly improved activity and stability compared to unsupported Ag.

These results highlight the dominant role of metal−support interactions in governing catalytic behavior. The ZrO_2 support stabilizes high-valent $Ag^{\delta+}$ species under anodic conditions, suppresses Ag dissolution, and enables sustained activity, as evidenced by XPS and electrochemical measurements. The MOF-derived Ag-ZrO_2 further amplifies this effect by maximizing the density of Ag-ZrO_2 interfacial sites through improved dispersion while maintaining a favorable particle size regime. Consequently, MOF-Ag-ZrO_2 exhibits the highest activity among the catalysts studied.

MEA System Optimization Enables Production of High FE and Concentration of EO

Ethylene oxide is known to have a lower separation energy than ethylene glycol. At 10 wt % in water, ethylene oxide (in light of its low 11 °C boiling point) exits a room-temperature electrolyzer in the gas phase and is estimated to require less than 5 GJ/ton_{EO} for separation. In contrast, EG, with its 197 °C boiling point, requires 50 GJ/ton_{EG} at this same product concentration, which also increases exponentially with lower product concentrations in aqueous electrolyte (Figure 4b, Supplementary note 2).

With the optimized MOF-Ag-ZrO_2 catalyst, we noted that there are considerable amounts of EO dissolved in the anolyte and being converted to EG, which takes up nearly 30% of the total products, leading to unwanted waste or large separation costs due to the diluted product in the electrolyte. We sought to pursue systems that would maximize EO product concentration, maximize FE to EO (and avoid EG), minimize product crossover, and minimize full cell voltage.

The high water concentration at the anode surface in the flow cell configuration leads to the fast dissolution of ethylene oxide into the anolyte at the gas−liquid interface. We herein sought to decrease the water content near the anode through the zero-gap MEA system using only a catholyte. The usage of anion and cation exchange membrane (AEM and CEM) systems led to different local environments compared with the flow cell. In an AEM system, we obtained 32% FE to ethylene oxide and collected highly concentrated ethylene oxide from the gas outlet with a lesser portion dissolved into the electrolyte, but the FE decreases due to the high OH^- flux near the anode that favors the OER (Figure S29). In a CEM system, FE_{EO} reached nearly 40%, but we also observed a higher ethylene glycol-to-ethylene oxide ratio formation than in the AEM system. This latter finding is assignable to the high proton concentration near the anode catalyst that accelerates the hydrolysis of EO to EG and its crossover to the catholyte, resulting in a lower total EO FE collected from the anode gas channel (Figure 4c and 4d, Figure S29).

Seeking to further improve the EO FE and lower the full cell potential, we moved to a microporous hydrophilic PTFE membrane—one that is not selective to a particular class of ion. We soaked it in 0.5 M $NaClO_4$ to form a solid electrolyte to separate the cathode and anode (Figure 4e). Varying the porosity and thickness of the membrane affects water permeability and performance. Our concept is that higher permeability could facilitate ion transport between the anode and cathode, thereby improving the overall ethylene oxidation FE and reducing the full cell voltage. To avoid ethylene oxide dissolution (similar to a flow cell) due to the higher water concentration near the anode, we sought to increase the thickness and decrease the pore size of the membrane to reduce the water content near the anode and suppress EO dissolution.

We then tested hydrophilic PTFE membranes with a range of porosities and thicknesses. We observed an increasing ethylene oxide FE from the gas outlet and lower dissolution into the electrolyte with decreasing porosity of the membrane, with the best performance achieved on 0.45 μm pore size PTFE and thickness around 60 μm (Figure 4f), with negligible hydrogen detected from the anode. Increasing the thickness of the PTFE membrane improved neither the FE nor the product concentration at the anode but instead led to slightly higher full-cell voltage due to the higher system resistance (Figure S30).

In the optimized system, we obtained 50% FE to ethylene epoxides at full cell voltage around 2.1 V, which is lower than in both CEM and AEM systems, achieving a productivity of 460 μmol cm^{-2} h^{-1} and a 0.5 V reduction compared to the most efficient prior report on olefin oxidation[9] (Figure 4c). 96% of the product on the anode was readily separable ethylene oxide, and only around 10% was found to have crossed over to the catholyte, with no hydrogen crossover to the anode observed (Figure S31). The system was then subjected to an extended stability test and showed stable performance, with FE consistently kept above 40% from the anode gas outlet for over 10 hours—more than 15 times that of the pristine Ag sample (Figure 4g and Figure S32). The ethylene oxide exiting the anode gas channel reached 48 ± 8 wt % among all the elements collected from the gas channel (Figure 4h).

When we carry out a technoeconomic analysis (details in SI), we find that at 50 mA/cm^2, FE 50%, and a measured 2.1 V full cell voltage, technoeconomic parity is achieved once electricity prices descend to 2 cents/kWh; and if green hydrogen can be sold for $5/kg and the ethylene feedstock costs $1000/ton (Figures S33 and S34).

■ CONCLUSIONS

Olefin oxidation to oxiranes and glycols represents an anodic pairing—an alternative to OER—of interest, both for the economic benefits of coupled electrolysis and for its increased amount of decarbonization per MWhr of electricity.[1,2] Ag, a thermocatalyst used in ethylene epoxidation, becomes stable in electrooxidation once it is impregnated into a metal support. ZrO_2 support stabilizes the Ag at its high oxidation states and suppresses Ag dissolution, and the Ag and ZrO_2 interface promotes the O* formation step that further facilitates the epoxidation rate. Moving from a redox mediator to a direct heterogeneous oxidation pathway enables systems to generate a concentrated product stream and minimizes separation costs. In an MEA system with microporous hydrophilic PTFE as the membrane, the Ag-ZrO_2 catalyst exhibited an ethylene oxide FE of 50% under a full cell voltage of 2.1 V at 50 mA/cm^2, with a productivity of 460 μmol cm^{-2} h^{-1} and a highly concentrated ethylene oxide stream of 48 wt % in the mixture exiting the anode gas channel.

■ MATERIALS AND METHODS

Chemicals

Zirconium(IV) chloride ($ZrCl_4$), Cerium(III) chloride heptahydrate ($CeCl_3 \cdot 7H_2O$), 2-Aminoterephthalic acid (BDC-NH_2), Dimethyl 2,6-pyridinedicarboxylate (NDC), *N*,*N*-dimethylformamide (DMF), Silver nitrate ($AgNO_3$), sulfuric acid (H_2SO_4), phosphoric acid (H_3PO_4), potassium phosphate monobasic (KH_2PO_4), potassium phosphate dibasic (K_2HPO_4), potassium hydroxide (KOH), and sodium perchlorate ($NaClO_4$), Hydrophilic PTFE membrane Omnipores were purchased from Sigma-Aldrich and used without further purification. The Nafion 115 membrane, Nafion D520 ionomer, Sustanion membrane, H23C8 gas diffusion electrode substrate, Pt mesh, and 60% platinum on carbon were purchased from Fuel Cell store. Deionized water (18.2 MΩ) was used for all the electrolytes preparation. The nitrogen (N_2) gas and ethylene (C_2H_4) gas were purchased from Linde Gas.

Catalyst Preparation Methods

CeO_2: $Ce(NO_3)_3 \cdot 6H_2O$ (6 mmol, 2.605 g) was dissolved in 60 mL distilled water and 6 g of NaOH was rapidly added with vigorous stirring. After 10 min of stirring, all of the admixtures were then transferred into a Teflon-lined stainless-steel autoclave and heated at 130 °C for 18 h. The products were collected by filtration, washed with distilled water to remove any possible ionic remnants, and then dried in a vacuum oven for at least 12 h, and calcined at 300 °C for 4 h.

ZrO_2: $ZrCl_4$ (6 mmol, 1.398 g) was dissolved in 60 mL dissolved water and 6 g of NaOH was rapidly added with vigorous stirring. After 10 min of stirring, all of the admixtures were then transferred into a Teflon-lined stainless steel autoclave at 130 °C for 18 h. The products were collected by filtration, washed with distilled water to remove any possible ionic remnants, and then dried in a vacuum oven for at least 12 h and calcined at 300 °C for 4 h.

The preparation of Ag-CeO_2/ZrO_2 with (20 wt % Ag): Solution A: Disperse the as-obtained 200 mg of ceria into 20 mL of DI water and sonicate for 30 min to make solution A. Then, slowly add solution B, which consists of 63.5 mg of $AgNO_3$ (40 mg of Ag) and 6 mL of DI-H_2O to solution A under stirring. By changing the mass of $AgNO_3$, catalysts with different Ag loadings can be obtained. Slowly drop solution C, which consists of 5 mL NH_4OH and 50 mL of DI-H_2O into the mixture of solution A and solution B. Keep pH = 10, then stir for 24 h. Wash the product with H_2O for three times and dry it in the oven. Anneal the sample at 250 °C in H_2 or air flow gas for 1 h (rate: 5 °C/min). We can change the loading amount of Ag (1−40 wt %) on different oxide materials (CeO_2, ZrO_2)

Synthesis of the Zr/MOF Template: The synthesis of Zr/MOF was modified from a literature-reported method. In detail, 4 mmol of $ZrCl_4$ and 2.5 mmol of linker ($BDC-NH_2$ and NDC in a 1:0.25 ratio) were dissolved in 24 mL of DMF. The suspension was then transferred into a hydrothermal reactor with a 50 mL Teflon-lined vessel. The synthesis was conducted in a 100 °C oven for 24 h. After cooling to room temperature naturally, the Zr/MOF was collected through centrifugation and washed with DMF three times and MeOH three times. The precipitates were then dried in a vacuum oven at 100 °C.

Preparation of Ag/ZrO_2: Silver was loaded onto the Zr/MOF through the incipient impregnation method. Taking 40% Ag loading as an example, in a 20 mL vial with an airtight cap, 0.35 mL of a silver precursor aqueous solution (0.9 g ($AgNO_3$)/1 mL) was added to 500 mg of as-synthesized Zr/MOF. The vial was immediately sealed, and the mixture was sonicated, followed by vigorous stirring to enable the uniform dispersion of the Ag precursor. After stirring for 12 h, the vial was left uncapped to enable the evaporation of the solvent. Mild heating (40−50 °C) could be applied to accelerate the drying process. The pyrolysis at 450 °C for 6 h under air converted the Ag-loaded Zr/MOF to the Ag-loaded ZrO_2 catalyst.

Electrochemical Cell Configurations

All of the electrochemical measurements were performed using an electrochemical station (Autolab PGSTATS204). The electrolytes used for the tests were 0.5 M sodium perchlorate aqueous solution. In H-cell tests, both the anode and cathode chambers each contained 25 mL of electrolyte; ethylene was bubbled into the anode chamber continuously at flow rates of around 15~20 sccm.

The glass H-cell setup has 3 electrodes: an electrodeposited catalyst on hydrophilic carbon paper as the working electrode, a Pt foil as the counter electrode, and an Ag/AgCl (3 M KCl) as the reference electrode. A cation exchange membrane (CEM, Nafion 115) was used to separate the anode and cathode chambers. Electrolytes in the anode and cathode chambers were agitated by using magnetic stirrers when needed.

The flow cell setup consisted of three chambers: the catholyte chamber, the anolyte chamber, and the gas flow chamber. The size of the electrode exposed to gas and anolyte had dimensions of 1 cm × 1 cm. The anode gas diffusion electrode (GDE) was positioned between the anolyte chamber and the gas flow chamber, with its substrate side facing the gas flow chamber and its catalyst side facing the anolyte chamber. A platinum (Pt) foil was used in the catholyte chamber as the counter electrode. The catholyte and anolyte chambers were separated by a cation exchange membrane (CEM, Nafion 115). An Ag/AgCl reference electrode, immersed in 3 M KCl, was placed in the anolyte chamber. Anolyte and catholyte solutions were introduced through separate silicone tubes by using peristaltic pumps at a constant flow rate of approximately 10 mL/min. The solutions entered each chamber from the bottom and exited from the top, recirculating back to their respective bulk electrolytes. For gas supply, a digital mass flow controller (SmartTrack 100, Sierra) was connected to a C_2H_4 gas cylinder to regulate the flow rate in the gas flow chamber.

The membrane electrode assembly (MEA) consists of two current collectors that are made of stainless steel and titanium for cathode and anode connections, respectively, with carved flow channels in the center area, with dimensions of 1 cm × 1 cm. The cathode is made by spraying Pt/C (60% Platinum on Vulcan XC-72R) on hydrophilic carbon paper. The anode is the catalyst prepared as illustrated in the manuscript. CEM (Nafion 115), AEM (Sustanion), and hydrophilic PTFE membranes are each used to separate the anode and cathode for the MEA performance tests. Catholyte is introduced through silicone tubes at a constant flow rate, the same as in the flow cell setup.

Material Characterizations

Scanning Transmission Electron Microscopy (STEM) characterizations were performed on a JEOL ARM 200CF microscope operated at 200 keV. The STEM image and FFT were processed with Gatan DigitalMicrograph. X-ray Energy Dispersive Spectroscopy (EDS) elemental mapping was collected with a dual SDD EDS detector and processed with Pathfinder software. X-ray Photoelectron Spectroscopy (XPS) measurements were conducted with a Thermo Fisher Scientific NEXSA G2 XPS instrument with a monochromated Al Kα X-ray source. N_2 physisorption was performed using a Micromeritics 3Flex at −196 °C. Catalyst composition was measured via ICP-OES on an Agilent 700 Series ICP-OES spectrometer operating in axial mode. ICP samples were prepared by dissolution in a diluted aqua regia solution. Raman tests were carried out using a Renishaw inVia Raman Microscope and an in situ lens with a water immersion objective (HCX APO L 63x/0.90 W UV Immersion). A custom-made cell was used to carry out *in situ* Raman spectroscopy. A laser wavelength of 532 nm was used as the excitation source. The laser power was kept at less than 0.20 mW in all experiments to minimize sample damage. The Raman spectrometer was calibrated with Si.

Gas Product Analysis

The gas products collected from the anodic outlet were analyzed by gas chromatography (PerkinElmer Clarus 680). The gas products were collected from the gas outlet channel of the flow cell and injected into a gas chromatograph (PerkinElmer Clarus 680). The gas chromatograph was equipped with a thermal conductivity detector (TCD) for the detection of H_2, O_2, N_2, and CO signals, and a flame ionization detector (FID) for the detection of CH_4 and C_2H_4 signals. The gas chromatograph was composed of packed columns of Molecular Sieve 5A and Carboxen-1000 and employed Argon (Linde, 99.999%) as the carrier gas. For quantification, 1 mL of gas product was injected into the gas chromatograph, and the performance was evaluated as a function of current density, gas flow rate, and gas product fractions.

The in situ EC-MS analysis was conducted by using a real-time applied electrochemical potential protocol with continuous monitoring of gas-phase products. Mass spectrometry was performed with a Hiden HPR-20 QIC Capillary system coupled with a customized electrochemical cell. All gaseous products were introduced into the capillary inlet and subsequently ionized. The ionization process was carried out at an electron potential of 70 V.

The resulting ions were detected using a secondary electron multiplier (SEM) detector, operating at a voltage of 800 V.

Liquid Product Analysis

^{1}H NMR spectroscopy (600 MHz Agilent DD2 NMR Spectrometer) is used to measure the content of ethylene oxide and ethylene glycol in the final electrolyte. The ethylene oxide and glycol are collected in both the anode gas chamber and the anolyte. The outlet of the anode gas chamber is connected to 10 mL of pure water inside a tube for dissolution and then tested. Dimethyl sulfoxide is used as the reference standard for quantifying the product, and D_2O is used as the solvent for the product. The Faradaic efficiency was calculated using the equation below:

$$\text{Faradaic efficiency (\%)} = N \times F \times n_{\text{product}}/Q$$

where N is the number of electrons transferred, F is the Faradaic constant, n_{product} is the total moles of products, and $Q = i \times t$ is the total charge passed during the experiment.

Internal standard solution: 35 mg of DMSO is first mixed into 5500 mg of D_2O (solution 1). Solution 1 is then further diluted, and 120 mg of solution 1 is mixed with 7800 mg of D_2O, which is the final reference standard solution. The exact weight of each chemical mentioned above might vary between different batches. In the final samples that are used for the NMR test, 100 μL of the reference standard solution is added to 600 μL of the final electrolyte, and the final concentration of DMSO in the solution is at the ppm level (3~5 ppm). The n_{product} and FE values are determined by analyzing the area ratio of the DMSO peaks relative to the characteristic peaks of the products.

COMPUTATIONAL METHODS

Spin-polarized density functional theory (DFT) calculations were conducted by using the Vienna Ab Initio Simulation Package (VASP). The Perdew−Burke−Ernzerhof (PBE) functional was applied to describe the exchange-correlation within the Kohn−Sham equation, and electron−ion interactions were described using the projector-augmented wave (PAW) method. Grimme's DFT-D3 method was utilized to account for long-range dispersion forces. Solvent effects were incorporated via the implicit solvent model, as implemented in VASPsol. The calculations used a kinetic energy cutoff of 450 eV and a 2 × 2 × 1 Monkhorst−Pack k-point grid for Brillouin-zone sampling. Structural relaxations were performed until residual forces were below 0.02 eV/Å, and energy convergence was achieved to within 10^{-5} eV.

We selected a five-layered AgO (111) supercell containing 80 Ag and 80 O atoms to represent the oxidized Ag surface. The AgO-ZrO_2 interface was modeled using a Zr_4O_8 cluster deposited on the AgO (111) supercell (Figure S13). This inverse modeling approach has been shown to effectively capture the structural motifs of metal/oxide surfaces. For all slabs, the atoms in the bottom two layers were fixed in their bulk positions, while the remaining atoms were allowed to relax. A vacuum layer of at least 15 Å was applied perpendicular to the surface to prevent interactions between periodic images.

ASSOCIATED CONTENT

Data Availability Statement

Data that support the findings of this study can be found in the article and Supporting Information. All other data supporting this work are available from the corresponding authors upon reasonable request.

Supporting Information

The Supporting Information is available free of charge at https://pubs.acs.org/doi/10.1021/jacs.5c17562.

> Faradaic efficiency and current density performance data with controlled samples and electrolyte; cyclic voltammetry curves; ^{1}H NMR spectra of all the ethylene oxidation products; additional Raman, XPS, and XRD spectra; electron microscope images of samples; computational models used for calculating the free energies of the reaction intermediates; three supplementary notes that include the details of techno-economic analysis, methods for Aspen Plus simulation for ethylene glycol and ethylene oxide separation, and the membrane and electrolyte effect analysis (PDF)

AUTHOR INFORMATION

Corresponding Authors

David Sinton − *Department of Mechanical and Industrial Engineering, University of Toronto, Toronto, Ontario M5S 3G8, Canada*; Email: david.sinton@utoronto.ca

Edward H. Sargent − *Department of Electrical and Computer Engineering, University of Toronto, Toronto, Ontario M5S 1A4, Canada; Department of Chemistry, Northwestern University, Evanston, Illinois 60208, United States; Department of Electrical and Computer Engineering, Northwestern University, Evanston, Illinois 60208, United States*; orcid.org/0000-0003-0396-6495; Email: ted.sargent@northwestern.edu

Authors

Jianan Erick Huang − *Department of Electrical and Computer Engineering, University of Toronto, Toronto, Ontario M5S 1A4, Canada; Department of Chemistry, Northwestern University, Evanston, Illinois 60208, United States; Department of Electrical and Computer Engineering, Northwestern University, Evanston, Illinois 60208, United States*; orcid.org/0000-0001-5872-3680

Chengqian Wu − *Department of Mechanical and Industrial Engineering, University of Toronto, Toronto, Ontario M5S 3G8, Canada*

Yiqing Chen − *Department of Chemistry, Northwestern University, Evanston, Illinois 60208, United States; Department of Electrical and Computer Engineering, Northwestern University, Evanston, Illinois 60208, United States*

Jiaqi Yu − *Department of Chemistry, Northwestern University, Evanston, Illinois 60208, United States; Department of Electrical and Computer Engineering, Northwestern University, Evanston, Illinois 60208, United States*; orcid.org/0000-0001-7412-2746

Yuanjun Chen − *Department of Chemistry, Northwestern University, Evanston, Illinois 60208, United States; Department of Electrical and Computer Engineering, Northwestern University, Evanston, Illinois 60208, United States*

Huajie Ze − *Department of Chemistry, Northwestern University, Evanston, Illinois 60208, United States; Department of Electrical and Computer Engineering, Northwestern University, Evanston, Illinois 60208, United States*

Jaerim Kim − *Department of Chemistry, Northwestern University, Evanston, Illinois 60208, United States;*

Department of Electrical and Computer Engineering, Northwestern University, Evanston, Illinois 60208, United States; orcid.org/0000-0003-1534-4044

Jinhong Wu − *Department of Mechanical and Industrial Engineering, University of Toronto, Toronto, Ontario M5S 3G8, Canada*

Yang Bai − *Department of Electrical and Computer Engineering, University of Toronto, Toronto, Ontario M5S 1A4, Canada;* orcid.org/0000-0002-1643-3770

Xiangyu Ma − *Department of Chemistry, Northwestern University, Evanston, Illinois 60208, United States; Department of Electrical and Computer Engineering, Northwestern University, Evanston, Illinois 60208, United States;* orcid.org/0000-0001-8692-0307

Roham Dorakhan − *Department of Electrical and Computer Engineering, University of Toronto, Toronto, Ontario M5S 1A4, Canada;* orcid.org/0000-0001-8104-7174

Bosi Peng − *Department of Chemistry, Northwestern University, Evanston, Illinois 60208, United States; Department of Electrical and Computer Engineering, Northwestern University, Evanston, Illinois 60208, United States*

Hongmin An − *Department of Chemistry, Northwestern University, Evanston, Illinois 60208, United States; Department of Electrical and Computer Engineering, Northwestern University, Evanston, Illinois 60208, United States*

Rui Kai Miao − *Department of Mechanical and Industrial Engineering, University of Toronto, Toronto, Ontario M5S 3G8, Canada*

Min Liu − *Department of Mechanical and Industrial Engineering, University of Toronto, Toronto, Ontario M5S 3G8, Canada;* orcid.org/0000-0003-0201-3553

Lizhou Fan − *Department of Electrical and Computer Engineering, University of Toronto, Toronto, Ontario M5S 1A4, Canada*

Sungjin Park − *Department of Electrical and Computer Engineering, University of Toronto, Toronto, Ontario M5S 1A4, Canada*

Ke Xie − *Department of Chemistry, Northwestern University, Evanston, Illinois 60208, United States; Department of Electrical and Computer Engineering, Northwestern University, Evanston, Illinois 60208, United States;* orcid.org/0000-0003-4220-272X

Complete contact information is available at:
https://pubs.acs.org/10.1021/jacs.5c17562

Author Contributions

[⊥]J.E.H., C.W., Y.C., and J.Y. contributed equally to this work

Notes

The authors declare no competing financial interest.

REFERENCES

(1) Leow, W. R.; Völker, S.; Meys, R.; Huang, J. E.; Jaffer, S. A.; Bardow, A.; Sargent, E. H. Electrified hydrocarbon-to-oxygenates coupled to hydrogen evolution for efficient greenhouse gas mitigation. *Nat. Commun.* **2023**, *14*, 1954.

(2) Boulamanti, A.; Moya, J. A. Energy efficiency and GHG emissions: Prospective scenarios for the Chemical and Petrochemical Industry. *European Union* **2017**.

(3) Yue, H.; Zhao, Y.; Ma, X.; Gong, J. Ethylene glycol: Properties, synthesis, and applications. *Chem. Soc. Rev.* **2012**, *41*, 4218−4244.

(4) Morgan, E.; Manwell, J.; McGowan, J. Wind-powered ammonia fuel production for remote islands: A case study. *Renewable Energy* **2014**, *72*, 51−61.

(5) Rebsdat, S.; Mayer, D. Ethylene Oxide. In *Ullmann's Encyclopedia Of Industrial Chemistry*; Wiley-VCH Verlag GmbH & Co., 2001.

(6) Guo, S.; Wang, C.; Li, H.; Li, T.; Liu, C.; Gao, Y.; Zhao, B. H.; Zhang, B. CeO2Modification Promotes the Oxidation Kinetics for Adipic Acid Electrosynthesis from KA Oil Oxidation at 200 mA cm−2. *Angew. Chem. Int. Ed.* **2025**, *64*, No. e202423432.

(7) Yan, M.; Yang, R.; Liu, C.; Gao, Y.; Zhang, B. In Situ Probing the Anion-Widened Anodic Electric Double Layer for Enhanced Faradaic Efficiency of Chlorine-Involved Reactions. *J. Am. Chem. Soc.* **2025**, *147*, 6698−6706.

(8) Chen, D.; Ding, Y.; Cao, X.; Wang, L.; Lee, H.; Lin, G.; Li, W.; Ding, G.; Sun, L. Highly Efficient Biomass Upgrading by a Ni−Cu Electrocatalyst Featuring Passivation of Water Oxidation Activity. *Angew. Chem. Int. Ed.* **2023**, *62*, No. e202309478.

(9) Sun, L.; Pan, X.; Xie, Y.-N.; Zheng, J.; Xu, S.; Li, L.; Zhao, G. Accelerated Dynamic Reconstruction in Metal−Organic Frameworks with Ligand Defects for Selective Electrooxidation of Amines to Azos Coupling with Hydrogen Production. *Angew. Chem. Int. Ed.* **2024**, *63*, No. e202402176.

(10) Parod, R. J. Ethylene oxide. In *Encyclopedia of Toxicology*; 2nd ed.; Elsevier, 2005.

(11) Leow, W. R.; et al. Chloride-mediated selective electrosynthesis of ethylene and propylene oxides at high current density. *Science* **2020**, *1233*, 1228−1233.

(12) Lum, Y.; et al. Tuning OH binding energy enables selective electrochemical oxidation of ethylene to ethylene glycol. *Nat. Catal.* **2020**, *3*, 14−22.

(13) Chung, M.; Jin, K.; Zeng, J. S.; Ton, T. N.; Manthiram, K. Tuning Single-Atom Dopants on Manganese Oxide for Selective Electrocatalytic Cyclooctene Epoxidation. *J. Am. Chem. Soc.* **2022**, *144*, 17416−17422.

(14) Huang, J. E.; et al. Selective Electrified Propylene-to-Propylene Glycol Oxidation on Activated Rh-Doped Pd. *J. Am. Chem. Soc.* **2024**, *146*, 8641−8649.

(15) Ke, J.; et al. Dynamically Reversible Interconversion of Molecular Catalysts for Efficient Electrooxidation of Propylene into Propylene Glycol. *J. Am. Chem. Soc.* **2023**, *145*, 9104−9111.

(16) Zheng, Z.; Qi, L.; Luan, X.; Zhao, S.; Xue, Y.; Li, Y. Growing highly ordered Pt and Mn bimetallic single atomic layers over graphdiyne. *Nat. Commun.* **2024**, *15*, 7331.

(17) Lin, X.; Zhou, Z.; Li, Q.-Y.; Xu, D.; Xia, S.-Y.; Leng, B.-L.; Zhai, G.-Y.; Zhang, S.-N.; Sun, L.-H.; Zhao, G.; et al. Direct Oxygen Transfer from H 2 O to Cyclooctene over Electron-Rich RuO 2 Nanocrystals for Epoxidation and Hydrogen Evolution. *Angew. Chem. Int. Ed.* **2022**, *61*, No. e202207108.

(18) Chung, M.; et al. Direct propylene epoxidation via water activation over Pd-Pt electrocatalysts. *Science* **2024**, *383*, 49−55.

(19) Özbek, M. O.; Van Santen, R. A. The mechanism of ethylene epoxidation catalysis. *Catal. Lett.* **2013**, *143*, 131−141.

(20) Carbonio, E. A.; et al. Are multiple oxygen species selective in ethylene epoxidation on silver? *Chem. Sci.* **2018**, *9*, 990−998.

(21) Liu, J.; Lu, S.; Ann, S.; Linic, S. Mechanisms of Ethylene Epoxidation Over Silver from Machine Learning-Accelerated First-Principles Modeling and Microkinetic Simulations. *ACS Catal.* **2023**, *13*, 8955−8962.

(22) Ke, J.; Zhao, J.; Chi, M.; Wang, M.; Kong, X.; Chang, Q.; Zhou, W.; Long, C.; Zeng, J.; Geng, Z. Facet-dependent electrooxidation of propylene into propylene oxide over Ag3PO4 crystals. *Nat. Commun.* **2022**, *13*, 932.

(23) Dong, H.; Luo, R.; Zhang, G.; Li, L.; Wang, C.; Sun, G.; Wang, H.; Liu, J.; Wang, T.; Zhao, Z.-J.; et al. Electrochemical epoxidation enhanced by C2H4 activation and hydroxyl generation at the Ag/SnO2 interface. *Nat. Commun.* **2025**, *16*, 1901.

(24) Li, A. Z.; et al. One-Step Electrochemical Ethylene-to-Ethylene Glycol Conversion over a Multitasking Molecular Catalyst. *J. Am. Chem. Soc.* **2024**, *146*, 5622−5633.

(25) Levin, M. E.; Mitschke, J.; Smith, S.; Chipman, P. I.; Singh, S. K.; Lenahan, R.; Frederick, T. S.; Gulledge, B. Kinetics for the sulfuric acid-catalyzed reactions of ethyleneoxide with water and ethylene glycols. *Process Saf. Prog.* **2024**, *43* (2), 388−414.

(26) Rosen, B. A.; et al. Ionic Liquid − Mediated Selective Conversion of CO 2 to CO at. *Science* **2011**, *334*, 643−644.

(27) Holewinski, A.; Idrobo, J. C.; Linic, S. High-performance Ag-Co alloy catalysts for electrochemical oxygen reduction. *Nat. Chem.* **2014**, *6*, 828−834.

(28) Dong, X. Y.; Gao, Z. W.; Yang, K. F.; Zhang, W. Q.; Xu, L. W. Nanosilver as a new generation of silver catalysts in organic transformations for efficient synthesis of fine chemicals. *Catal. Sci. Technol.* **2015**, *5*, 2554−2574.

(29) Pu, T.; et al. Revealing the Nature of Active Oxygen Species and Reaction Mechanism of Ethylene Epoxidation by Supported Ag/α-Al2O3 Catalysts. *ACS Catal.* **2024**, *14*, 406−417.

(30) Alzahrani, H. A.; Bravo-Suárez, J. J. In situ Raman spectroscopy study of silver particle size effects on unpromoted Ag/α-Al2O3 during ethylene epoxidation with molecular oxygen. *J. Catal.* **2023**, *418*, 225−236.

(31) Pu, T.; et al. Nature and Reactivity of Oxygen Species On/In Silver Catalysts During Ethylene Oxidation. *ACS Catal.* **2022**, *12*, 4375−4381.

(32) Liu, C.; et al. Computational and experimental insights into reactive forms of oxygen species on dynamic Ag surfaces under ethylene epoxidation conditions. *J. Catal.* **2022**, *405*, 445−461.

(33) Cargnello, M.; et al. Control of Metal Nanocrystal Size Reveals Metal-Support Interface Role for Ceria Catalysts. *Science* **2013**, *341*, 771−773.

(34) Xing, F.; Nakaya, Y.; Yasumura, S.; Shimizu, K.; Furukawa, S. Ternary platinum−cobalt−indium nanoalloy on ceria as a highly efficient catalyst for the oxidative dehydrogenation of propane using CO2. *Nat. Catal.* **2022**, *5*, 55−65.

(35) Oh, H.; et al. Electrochemical Catalyst − Support Effects and Their Stabilizing Role for IrO x Nanoparticle Catalysts during the Oxygen Evolution Reaction. *J. Am. Chem. Soc.* **2016**, *138*, 12552−12563.

(36) Ren, Z.; et al. Pt/ZrO2 catalyst with metal-support synergistic effect towards glycerol selective oxidation. *Chem. Eng. J.* **2023**, *468*, 143623.

(37) Wang, T.; Hu, J.; Ouyang, R.; Wang, Y.; Huang, Y.; Hu, S.; Li, W.-X. Nature of metal-support interaction for metal catalysts on oxide supports. *Science* **2024**, *386*, 915−920.

(38) van Deelen, T. W.; Hernández Mejía, C.; de Jong, K. P. Control of metal-support interactions in heterogeneous catalysts to enhance activity and selectivity. *Nat. Catal.* **2019**, *2*, 955−970.

(39) Tanabe, K. Surface and catalytic properties of ZrO2. *Mater. Chem. Phys.* **1985**, *13*, 347−364.

(40) Nie, L.; et al. Activation of surface lattice oxygen in single-atom Pt/CeO2 for low-temperature CO oxidation. *Science* **2017**, *358*, 1419−1423.

(41) Grimaud, A.; Diaz-Morales, O.; Han, B.; Hong, W. T.; Lee, Y.-L.; Giordano, L.; Stoerzinger, K. A.; Koper, M. T. M.; Shao-Horn, Y. Erratum: Activate lattice oxygen redox reactions in metal oxides to catalyse oxygen evolution. *Nat. Chem.* **2017**, *9*, 457−465.